Particles I

Access the latest eBook →

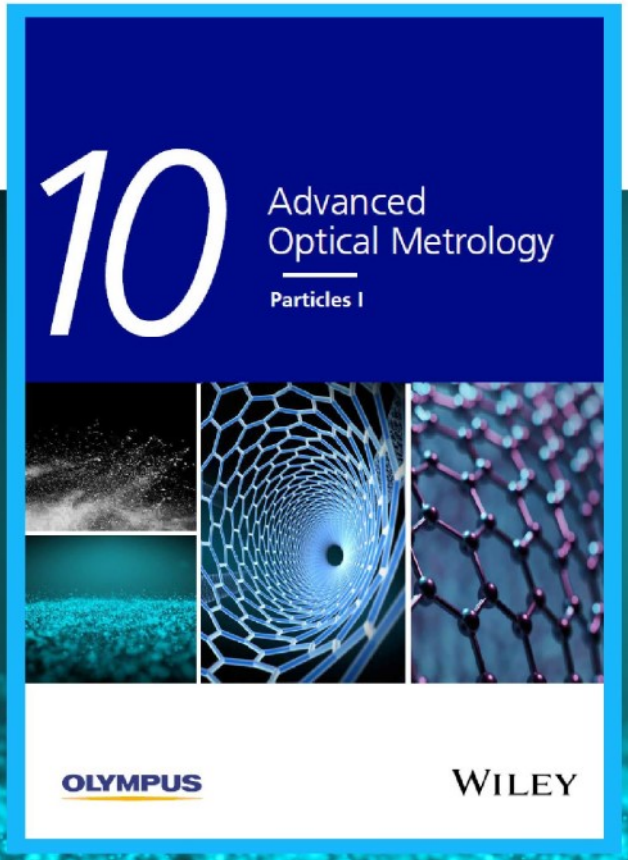

Particles: Unique Properties, Uncountable Applications

Read the latest eBook and better your knowledge with highlights from the recent studies on the design and characterization of micro- and nanoparticles for different application areas.

Access Now

This eBook is sponsored by

OLYMPUS

WILEY

small methods
www.small-methods.com

Defective Fe_3O_{4-x} Few-Atom Clusters Anchored on Nitrogen-Doped Carbon as Efficient Oxygen Reduction Electrocatalysts for High-Performance Zinc–Air Batteries

Panpan Chu, Yingmeng Zhang, Jiajie He, Jinhong Chen, Jingjun Zhuang, Yongliang Li, Xiangzhong Ren, Peixin Zhang, Lingna Sun, Bingzhe Yu, and Shaowei Chen**

It remains a challenge to develop cost-effective, high-performance oxygen electrocatalysts for rechargeable metal–air batteries. Herein, zinc-mediated zeolitic imidazolate frameworks are exploited as the template and nitrogen and carbon sources, onto which is deposited a Fe_3O_4 layer by plasma-enhanced atomic layer deposition. Controlled pyrolysis at 1000 °C leads to the formation of high density of Fe_3O_{4-x} few-atom clusters with abundant oxygen vacancies deposited on an N-doped graphitic carbon framework. The resulting nanocomposite (Fe_3O_{4-x}/NC-1000) exhibits a markedly enhanced electrocatalytic performance toward oxygen reduction reaction in alkaline media, with a remarkable half-wave potential of +0.930 V versus reversible hydrogen electrode, long-term stability, and strong tolerance against methanol poisoning, in comparison to samples prepared at other temperatures and even commercial Pt/C. Notably, with Fe_3O_{4-x}/NC-1000 as the cathode catalyst, a zinc–air battery delivers a high power density of 158 mW cm^{-2} and excellent durability at 5 mA cm^{-2} with stable 2000 charge–discharge cycles over 600 h. This is ascribed to the ready accessibility of the Fe_3O_{4-x} catalytic active sites, and enhanced electrical conductivity, oxygen adsorption, and electron-transfer kinetics by surface oxygen vacancies. Further contributions may arise from the highly conductive and stable N-doped graphitic carbon frameworks.

1. Introduction

Development of clean and renewable energy technologies is a critical step toward a sustainable future.[1] Among these, metal–air batteries represent a viable option. In particular, zinc–air battery (ZAB) has emerged as a next-generation green energy technology, due to the abundant zinc source, low cost, high safety, and a superb theoretical energy density (1086 Wh kg^{-1}).[2] However, the practical applications of ZAB have been impeded by the sluggish kinetics and high overpotentials of the oxygen evolution/reduction reactions (OER/ORR) at the cathode.[3] Noble metal-based nanoparticles (e.g., Pt, Pd, Ru, and Ir) have been the electrocatalysts of choice for ORR/OER,[4] but their natural scarcity, high cost, and low stability significantly limit the widespread application of the technology.

Thus far, extensive research has demonstrated that carbon-based composites with non-precious metals (such as Fe, Co, and Ni) and their oxides/sulfides/nitrides/carbides can serve as effective alternatives.[5] Among these, iron-based oxides have attracted much attention due to their excellent ORR performance in both acidic and alkaline media,[6] which can be readily prepared via pyrolysis of select iron salts at high temperatures.[7] However, agglomeration typically occurs without a supporting template, leading to a loss of active species. Therefore, anchoring iron-containing precursors into carbon framework substrates is critical in the preparation of highly active and durable electrocatalysts.[8]

In recent years, metal-organic framework (MOF) materials have been used extensively as structural templates and carbon precursors.[9] In particular, zeolite imidazole framework (ZIF), with a high nitrogen and carbon content, has been attracting unique attention due to the structural tunability, morphological diversity, and porosity.[10] In fact, a range of iron-containing composite catalysts have been prepared based on ZIF precursors by, for instance, solution precipitation[11] and ion exchange methods.[12] However, in such syntheses, as aggregation of the iron-containing compounds inevitably occurs within ZIF, the uneven distribution can significantly impact the morphology of the ZIF and eventual carbon composites, and part of the metal species becomes buried within the carbon matrix and inaccessible, both of which may compromise the proton and electron transfer in the electrocatalytic process and hence the electrocatalytic performance.[13]

P. Chu, Y. Zhang, J. He, J. Chen, J. Zhuang, Y. Li, X. Ren, P. Zhang, L. Sun
College of Chemistry and Environmental Engineering
Shenzhen University
Shenzhen, Guangdong 518060, P. R. China
E-mail: sunln@szu.edu.cn
B. Yu, S. Chen
Department of Chemistry and Biochemistry
University of California
Santa Cruz, CA 95064, USA
E-mail: shaowei@ucsc.edu

The ORCID identification number(s) for the author(s) of this article can be found under https://doi.org/10.1002/smtd.202200207.

DOI: 10.1002/smtd.202200207

Such an issue can be mitigated by atomic layer deposition (ALD), which can accurately control the uniform dispersion of functional components on substrate surfaces, and effectively reduce agglomeration.[14] In addition, the active materials are deposited onto the substrate surface and can be readily accessible for electrocatalysis.[15] Generally, ALD involves a sequential vacuum evaporation procedure with saturated and self-limiting reactions, and can not only be used to deposit metal oxides, nitrides, sulfides, and pure elements on substrates but also control the thickness of the deposition layer at the atomic level.[16] In catalyst preparation, the deposition can be precisely optimized by tailoring the ALD parameters and modifying the matrix substrate for a controllable structure and uniform nanoparticle dispersion, such that the catalyst loading can be minimized and the stability maximized. Indeed, ALD has been an effective synthesis method in the field of electrocatalysis,[16b] where precious/non-precious metals as well as their oxides, sulfides, and phosphides have been deposited onto a variety of substrates (e.g., nickel foam and carbon cloth), and used as effective catalysts toward a range of important reactions in electrochemical energy technologies.[16–17]

In the present study, a series of novel nanocomposites (Fe_3O_{4-x}/NC) were synthesized where defective Fe_3O_{4-x} few-atom clusters were anchored onto a nitrogen-doped graphitic carbon substrate by controlled pyrolysis of Fe_3O_4-coated ZIF that was obtained via plasma-enhanced ALD (PE-ALD). Among the series, the sample prepared at 1000 °C (Fe_3O_{4-x}/NC-1000) exhibited an outstanding ORR activity in both alkaline and acidic media with long-term stability and excellent methanol tolerance. Such a performance was markedly better than those in the sample series prepared at other temperatures and even commercial Pt/C. Remarkably, a zinc–air battery with Fe_3O_{4-x}/NC-1000 as the air cathode catalyst showed a high specific capacity of 691 mAh g^{-1}, power density of 158 mW cm^{-2}, and excellent durability. The remarkable ORR and zinc–air battery performance of the Fe_3O_{4-x}/NC-1000 composite was ascribed to the uniform dispersion of Fe_3O_{4-x} on the N-doped graphitic carbon framework whereby high-density active sites were fully exposed and readily accessible, enhanced electrical conductivity and electron-transfer kinetics by abundant oxygen vacancies, and highly conductive proton and electron transfer networks by the N-doped graphitic carbon framework.

2. Results and Discussion

2.1. Catalyst Synthesis and Structural Characterizations

The procedure of sample preparation is depicted in **Figure 1**, which entails three major steps: Chemical synthesis of ZIF precursor, PE-ALD deposition of Fe_3O_4 on ZIF, and finally pyrolysis of ZIF@Fe_3O_4 to yield Fe_3O_{4-x}/NC. The experimental details are included in the Supporting Information. First, the ZIF precursor was prepared by a simple coprecipitation method, which exhibited a smooth blade shape (Figure S1, Supporting Information). Then, a layer of Fe_3O_4 at a controlled thickness was deposited onto the ZIF surface by using the PE-ALD method with ferrocene as the iron source. Scanning electron microscopy (SEM) studies show that after 200 cycles of deposition the resulting ZIF@Fe_3O_4 surface became markedly roughened, with Fe_3O_4 nanoparticles homogeneously distributed on the ZIF surface (Figure S2, Supporting Information). The microstructure of ZIF@Fe_3O_4 was further examined by transmission electron microscopy (TEM) measurements, where the nanoparticles can be seen to exhibit well-defined lattice fringes with an interplanar spacing of 0.253 nm, corresponding to the (311) crystal planes of Fe_3O_4 (Figure S3, Supporting Information).[17a] Yet, the X-ray diffraction (XRD) patterns of ZIF@Fe_3O_4 were consistent with those of the ZIF precursor (Figure S4, Supporting Information), with no additional peaks for Fe_3O_4 likely due to the small size and low content of Fe_3O_4 on the ZIF surface.[18] Finally, pyrolysis at an elevated temperature in an argon atmosphere effectively transformed ZIF@Fe_3O_4 into Fe_3O_{4-x}/NC (denoted as Fe_3O_{4-x}/NC-T with T being the pyrolysis temperature).

As shown in the SEM images in **Figure 2**a and Figure S5, Supporting Information, the Fe_3O_{4-x}/NC-1000 sample retained the 2D leaf-like morphology of the ZIF@Fe_3O_4 precursor. Yet in high-resolution TEM (HRTEM) studies, no lattice fringes can be identified in Fe_3O_{4-x}/NC-1000 (Figure 2b,c), suggesting a largely amorphous structure and the formation of quasi-atomic Fe_3O_{4-x} structures. In fact, the selected area electron diffraction (SAED) patterns of Fe_3O_{4-x}/NC-1000 exhibited only the (002) and (100) electron diffraction rings of the graphitic carbon (Figure 2c inset). Consistent results were obtained in XRD measurements (Figure 2d), where Fe_3O_{4-x}/NC-1000 and Fe-free NC-1000 (prepared in the same fashion except for the PE-ALD deposition of Fe_3O_4) both showed only two broad diffraction

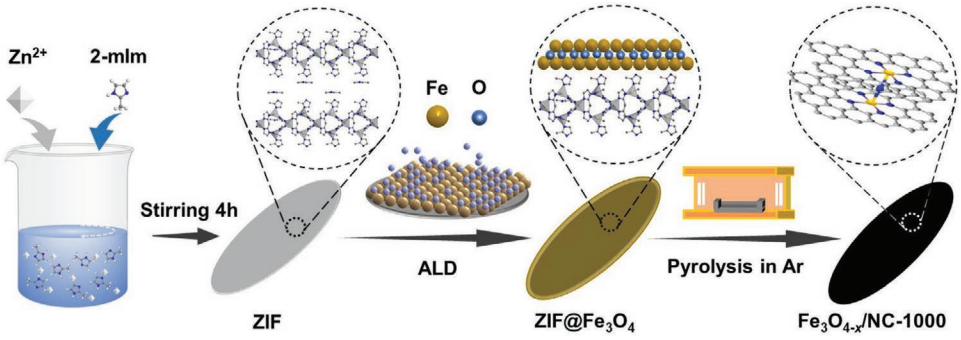

Figure 1. Schematic illustration of the preparation of Fe_3O_{4-x}/NC nanocomposites: synthesis of leaf-shaped ZIF precursors, PE-ALD deposition of Fe_3O_4 films on ZIF surface, and pyrolytic treatment.

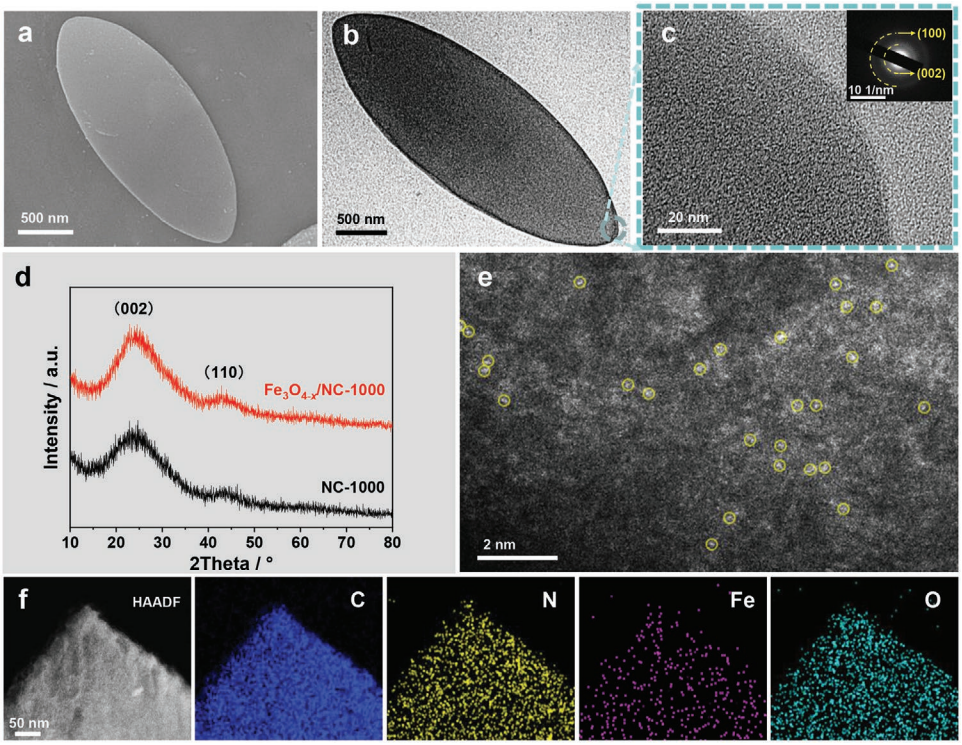

Figure 2. a) SEM and b,c) HRTEM images of Fe_3O_{4-x}/NC-1000. Inset in panel (c) is the corresponding selected area electron diffraction patterns. d) XRD patterns of Fe_3O_{4-x}/NC-1000 and NC-1000. e) HAADF-STEM image of Fe_3O_{4-x}/NC-1000 and f) the corresponding EDS-based elemental maps of Fe_3O_{4-x}/NC-1000.

peaks at $2\theta = 26.0°$ and 43.2°, corresponding to the (002) and (100) lattice planes of graphitic carbons, respectively.[13] Similar XRD patterns were obtained with samples prepared at other temperatures (i.e., 800, 900, and 1100 °C) (Figure S6, Supporting Information), again, confirming the low content of Fe compounds in the composites, which was quantitatively assessed to be approximately 0.25 wt% by inductively coupled plasma-mass spectrometry (ICP-MS) measurements. In high-angle annular dark field scanning transmission electron microscopy (HAADF-STEM) (Figure 2e), the Fe_3O_{4-x}/NC-1000 sample can indeed be seen to consist of a number of few-atom clusters, as highlighted by the yellow circles. Moreover, elemental mapping analysis based on energy-dispersive X-ray spectroscopy (EDS) shows that the Fe, C, N, and O elements were all uniformly dispersed across the carbon scaffold (Figure 2f).

In Raman spectroscopy measurements (Figure S7, Supporting Information), the Fe_3O_{4-x}/NC-1000 and Fe-free NC-1000 samples both featured two prominent vibrational bands at ≈1590 cm^{-1} and 1330 cm^{-1}, due to the G band (graphitic sp^2 carbon) and D band (disordered or defect carbon),[2c,19] respectively, with a close peak intensity ratio (I_D/I_G), 2.96 for Fe_3O_{4-x}/NC-1000 and 2.71 for NC-1000.[20] Similar I_D/I_G ratios were obtained for other samples, 3.36 for Fe_3O_{4-x}/NC-800, 2.98 for Fe_3O_{4-x}/NC-900, and 2.92 for Fe_3O_{4-x}/NC-1100. These suggest successful graphitization of the ZIF precursor by pyrolysis within the temperature range of 800 to 1100 °C.

X-ray photoelectron spectroscopy (XPS) was then used to further analyze the chemical compositions and valence states of the samples. From the survey spectrum in Figure S8a, Supporting Information, the elements of C, N, O, and Fe can be readily identified in Fe_3O_{4-x}/NC-1000 at ≈284, 401, 532, and 714 eV, with the contents of 90.53, 4.33, 4.84 and 0.30 wt% (Table S1, Supporting Information), respectively, consistent with results from elemental mapping analysis (Figure 1e). Note that the metal content is also in good agreement with that (0.25 wt%) from ICP-MS measurements. The corresponding high-resolution C 1s spectrum is depicted in Figure S8b, Supporting Information, which can be deconvoluted into three species, C=C (284.8 eV), C–N (285.7 eV), and C–O (286.9 eV), confirming the pyrolytic transformation of ZIF to graphitic carbon and successful doping of N into the carbon framework.[21] Consistent results were obtained in the deconvolution of the N 1s spectrum (Figure S8c, Supporting Information) which yielded four peaks, pyridine-N (398.6 eV), pyrrolic-N/metal-N (400.0 eV), graphene-N (401.0 eV), and oxidation-N (402.3 eV).[15,22] Similar behaviors were observed with Fe_3O_{4-x}/NC-800, Fe_3O_{4-x}/NC-900, and Fe_3O_{4-x}/NC-1100 (Figure S9a–c, Supporting Information). Notably, the N content exhibited a clear decline with increasing pyrolysis temperature, Fe_3O_{4-x}/NC-800 (13.61 wt%) > Fe_3O_{4-x}/NC-900 (10.72 wt%) > Fe_3O_{4-x}/NC-1000 (2.88 wt%) ≥ Fe_3O_{4-x}/NC-1100 (2.86 wt%), and graphitic N became the dominant species in the high-temperature samples of Fe_3O_{4-x}/NC-1000 and Fe_3O_{4-x}/NC-1100 (Figure S9d, Supporting Information). The O 1s spectrum of Fe_3O_{4-x}/NC-1000 is shown in **Figure 3**a, which can be deconvoluted into four peaks, adsorbed hydroxyl (Fe–O–H bonds) at 531.9 eV,[23] carboxyl at 532.6 eV, adsorbed water at 533.8 eV,[24] and Fe–O bonds at 530.8 eV (Figure S9e–h, Supporting Information).[24] The Fe 2p spectrum is shown in Figure 3b, where deconvolution yields two doublets. The first pair at 710.1/722.8 eV can be attributed to the

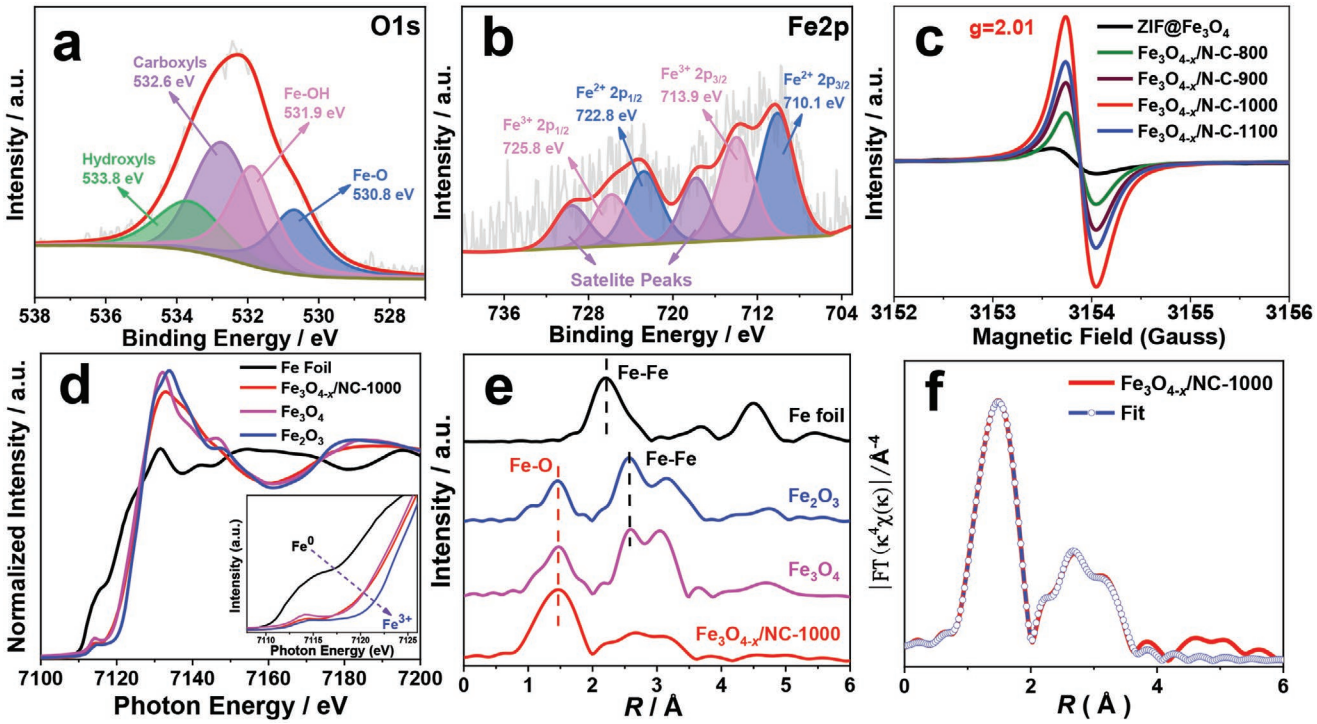

Figure 3. High-resolution XPS spectra of the a) O 1s and b) Fe 2p electrons of Fe_3O_{4-x}/NC-1000. c) Electron paramagnetic resonance spectra of ZIF@Fe_3O_4, Fe_3O_{4-x}/NC-800, Fe_3O_{4-x}/NC-900, Fe_3O_{4-x}/NC-1000, and Fe_3O_{4-x}/NC-1100. d) Fe K-edge XANES spectra of Fe_3O_{4-x}/NC-1000, Fe foil, Fe_3O_4, and Fe_2O_3 with a zoomed-in view of the pre-edge regions in the inset. e) Fourier-transformed (FT) EXAFS of Fe_3O_{4-x}/NC-1000, Fe foil, Fe_3O_4, and Fe_2O_3. f) FT-EXAFS fitting curves in *R* space of Fe_3O_{4-x}/NC-1000.

$2p_{2/3}/2p_{1/2}$ electrons of Fe^{2+},[25] whereas the other at 713.9/725.8 eV to those of Fe^{3+} (the peaks near 717.0 eV and 728.5 eV are the corresponding Fe satellite peaks).[26] This suggests the formation of iron oxide compounds within the carbon nanocomposites.

Consistent results were obtained in electron-paramagnetic resonance (EPR) measurements (Figure 3c), where the series of samples can be seen to exhibit a clearly defined signal within the range of 3152 and 3156 G, with $g = 2.01$, in good agreement with electrons trapped in oxygen vacancies.[24a,27] Yet, the peak-to-peak amplitude increases in the order of ZIF@Fe_3O_4 < Fe_3O_{4-x}/NC-800 < Fe_3O_{4-x}/NC-900 < Fe_3O_{4-x}/NC-1100 < Fe_3O_{4-x}/NC-1000, suggesting that the oxygen vacancy concentration was the highest in Fe_3O_{4-x}/NC-1000 among the series. The structural and electronic characteristics of the Fe centers were further examined by X-ray absorption spectroscopy measurements. The Fe K-edge X-ray absorption near-edge structures (XANES) are depicted in Figure 3d and inset, where the Fe_3O_{4-x}/NC-1000 sample can be seen to exhibit an absorption edge and pre-edge peak (at ≈ 7114 eV due to the 1s → 3d transition arising from the 3d orbital splitting of Fe atoms and the local coordination between Fe and O)[28] very close to that of Fe_3O_4 and between those of Fe foil and Fe_2O_3.[28] This suggests that the Fe valence state in Fe_3O_{4-x}/NC-1000 is between Fe^0 and Fe^{3+},[29] consistent with the XPS results (Figure 3b).

Figure 3e shows the corresponding Fourier-transform Fe K-edge extended X-ray absorption fine structures (EXAFS) spectra. The Fe_3O_{4-x}/NC-1000 sample can be observed to display a profile that is consistent with those of Fe_2O_3 and Fe_3O_4 but markedly different from that of Fe foil, featuring a predominant peak at 1.47 Å and a broad peak between 2.0 and 3.5 Å. The former can be ascribed to the Fe–O/N coordination bond, whereas the latter is likely due to the Fe–Fe shell in the oxides. Notably, the fact that Fe_3O_{4-x}/NC-1000 possessed a drastically weakened Fe–Fe shell, in comparison to Fe_3O_4 and Fe_2O_3, is consistent with the formation of Fe few-atom clusters dispersed in the N-doped graphitic carbon matrix (Figure 2e). Figure 3f shows the fitting of the EXAFS curves in *R* space, and the corresponding *k*-space fitting is included in Figure S10, Supporting Information, (note that the latter is very similar to that of Fe_3O_4). Notably, from Table S2, Supporting Information, one can see that the number of O atoms coordinated to Fe is estimated to be 4.6 with a Fe–O bond length of 1.99 Å, which is close to that of Fe_3O_4 with oxygen vacancy (4.5), but lower than that of pristine Fe_3O_4 (4.9), and the coordination numbers of the Fe–O–Fe path (3.1, 1.5) are also close to those of defective Fe_3O_4 (4.0, 1.3), while lower than those of pristine Fe_3O_4 (5.0, 3.8).[23c]

Taken together, results from these microscopic and spectroscopic measurements suggest the formation of defective Fe_3O_{4-x} few-atom clusters within the nanocomposites, and the Fe_3O_{4-x}/NC-1000 sample contained the highest concentration of oxygen vacancies among the series. This corresponds to the optimal ORR activity, as manifested below.

2.2. Electrocatalytic Activity

The electrocatalytic activity of the produced nanocomposites was then assessed and compared in 0.1 M KOH using a rotating

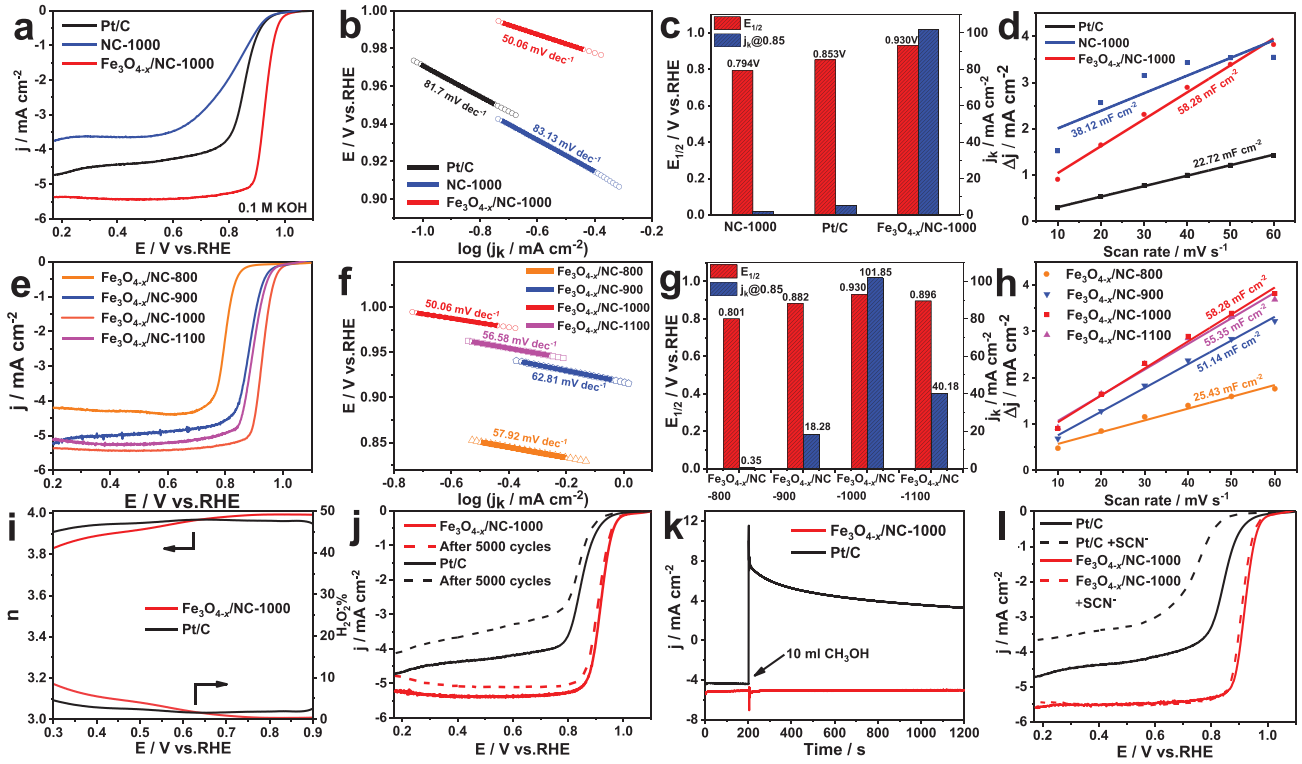

Figure 4. ORR performance of Fe_3O_{4-x}/NC-1000, commercial Pt/C, and NC-1000 in O_2-saturated 0.1 M KOH at a rotation rate of 1600 rpm and potential scan rate of 5 mV s^{-1}: a) Polarization curves, b) corresponding Tafel plots, and c) kinetic current density (j_k, at +0.85 V) and half-wave potential ($E_{1/2}$). d) Double-layer capacitance (C_{dl}) of Fe_3O_{4-x}/NC-1000, commercial Pt/C, and NC-1000 calculated from CV measurements at scan rates from 10 to 60 mV s^{-1}. Comparative ORR performance of Fe_3O_{4-x}/NC-800, Fe_3O_{4-x}/NC-900, Fe_3O_{4-x}/NC-1000, and Fe_3O_{4-x}/NC-1100: e) polarization curves, f) corresponding Tafel plots, g) kinetic current density (j_k, at +0.85 V) and half-wave potential ($E_{1/2}$), and h) double-layer capacitance (C_{dl}). i) Number of electron transfer (n) and the percentage of peroxide (H_2O_2%) produced on Fe_3O_{4-x}/NC-1000 and commercial Pt/C. j) ORR polarization curves of Fe_3O_{4-x}/NC-1000 and commercial Pt/C before and after 5000 cycles between +0.6 and +1.0 V at a scan rate of 100 mV s^{-1}. k) Chronoamperometric profiles at +0.75 V after the introduction of 10 mL methanol into 160 mL of a 0.1 M KOH solution for Fe_3O_{4-x}/NC-1000 and commercial Pt/C. l) Linear sweep voltammogram curves of Fe_3O_{4-x}/NC-1000 and commercial Pt/C with and without 10 mmol SCN^- at a rotation rate of 1600 rpm with a scan rate of 5 mV s^{-1}.

ring-disk electrode (RRDE). In cyclic voltammetric (CV, Figure S11, Supporting Information) measurements, both Fe_3O_{4-x}/NC and commercial Pt/C can be seen to exhibit an obvious reduction peak when the electrolyte solution was saturated with O_2, whereas only a featureless profile was observed with a N_2-purged solution, indicating electrocatalytic activity toward ORR.[30] In RRDE measurements (**Figure 4**a), Fe_3O_{4-x}/NC-1000 displays an excellent ORR activity with an onset potential (E_{onset}) of ≈ +1.010 V versus reversible hydrogen electrode (RHE) and half-wave potential ($E_{1/2}$) of +0.930 V, which is much higher than those of commercial Pt/C (E_{onset} = +0.989 V, $E_{1/2}$ = +0.852 V), Fe-free NC-1000 (E_{onset} = +0.867 V, $E_{1/2}$ = +0.794 V), and the ZIF@Fe_3O_4 precursor (Figure S12, Supporting Information). These results suggest that the vacancy-rich Fe_3O_{4-x} played a vital role in ORR electrocatalysis. Samples prepared at other calcination temperatures also exhibited an apparent ORR activity (Figure 4e), with E_{onset} = +0.897 V and $E_{1/2}$ = +0.800 V for Fe_3O_{4-x}/NC-800, +0.995 and +0.883 V for Fe_3O_{4-x}/NC-900, and +0.992 and +0.899 V for Fe_3O_{4-x}/NC-1100, suggesting that 1000 °C was the optimal pyrolysis temperature within the present experimental context.

From the Tafel plots in Figure 4b,f, one can see that Fe_3O_{4-x}/NC-1000 possessed the lowest Tafel slope (50.06 mV dec^{-1}), in comparison to Fe_3O_{4-x}/NC-1100 (56.58 mV dec^{-1}), Fe_3O_{4-x}/NC-900 (62.81 mV dec^{-1}), Fe_3O_{4-x}/NC-800 (57.92 mV dec^{-1}), commercial Pt/C (81.70 mV dec^{-1}), and Fe-free NC-1000 (83.13 mV dec^{-1}). This again confirmed that Fe_3O_{4-x}/NC-1000 stood out as the best ORR catalyst among the sample series. In fact, as shown in Figure 4c,g, Fe_3O_{4-x}/NC-1000 achieved a kinetic current density (j_k) of 101.85 mA cm^{-2} at +0.85 V, much better than Fe_3O_{4-x}/NC-1100 (40.18 mA cm^{-2}), Fe_3O_{4-x}/NC-900 (18.28 mA cm^{-2}), Fe_3O_{4-x}/NC-800 (0.35 mA cm^{-2}), commercial Pt/C (5 mA cm^{-2}), and Fe-free NC-1000 (2 mA cm^{-2}).

Notably, the double-layer capacitance (C_{dl}) of Fe_3O_{4-x}/NC-1000 was evaluated to be 29.14 mF cm^{-2}, markedly larger than those of commercial Pt/C (11.36 mF cm^{-2}), NC-1000 (19.06 mF cm^{-2}) (Figure 4d and Figure S13a–c, Supporting Information), Fe_3O_{4-x}/NC-800 (12.71 mF cm^{-2}), Fe_3O_{4-x}/NC-900 (25.57 mF cm^{-2}), and Fe_3O_{4-x}/NC-1100 (27.67 mF cm^{-2}) (Figure 4h and Figure S13d–f, Supporting Information). This suggests a maximum electrochemical surface area in Fe_3O_{4-x}/NC-1000 among the sample series, a unique feature conducive to the accessibility of electrocatalytic active sites.

In addition, based on the disk and ring currents, the average number (n) of electron transfer of Fe_3O_{4-x}/NC-1000 was estimated to be 3.82–3.99 within the wide potential range

of +0.3 to +0.9 V (Figure 4i), close to that of commercial Pt/C (3.90–3.95). Similar results were obtained from the slopes of the Koutecky–Levich (K-L) plots (Figure S14, Supporting Information). In addition, the corresponding hydrogen peroxide (H_2O_2) yield is found to be under 9% with the Fe_3O_{4-x}/NC-1000 sample, which was rather comparable to that of Pt/C (Figure 4i).

Apart from catalytic activity, durability is also an important factor in practical applications. As shown in Figure S15, Supporting Information, chronoamperometric (i-t) tests were carried out for 10 h under a constant potential of +0.75 V versus RHE, and Fe_3O_{4-x}/NC-1000 can be seen to retain 88.16% of the initial current, far better than commercial Pt/C (76.87%). The catalyst stability was also evaluated by potential cycling at the high sweep rate of 100 mV s^{-1} in O_2-saturated 0.1 M KOH within the potential range of +0.4 to +1.0 V (Figure 4j). After 5000 CV cycles, a small negative shift of 8 mV is observed for the $E_{1/2}$ of Fe_3O_{4-x}/NC-1000 (Figure 4j), in comparison to 12 mV for commercial Pt/C, further confirming the superb durability of Fe_3O_{4-x}/NC-1000.

Fe_3O_{4-x}/NC-1000 also demonstrated remarkable tolerance against methanol. In the chronoamperometric test (Figure 4k), after the injection of 10 mL methanol into a saturated-O_2 0.1 M KOH solution, the current density of commercial Pt/C decreased rapidly, while Fe_3O_{4-x}/NC-1000 maintained a relatively stable current density. The Fe_3O_{4-x}/NC-1000 also showed only a slightly reduced i-t response upon the addition of poisoning KSCN (10 mmol) into O_2-saturated 0.1 M KOH (Figure 4l), whereas the activity of commercial Pt/C was significantly diminished.

The ORR performance of Fe_3O_{4-x}/NC-1000 was also studied by RRDE in acidic media (Figures S16 and S17, Supporting Information). Whereas the performance was slightly subpar as compared to that of Pt/C, it remained markedly better than those of Fe_3O_{4-x}/NC-1100, Fe_3O_{4-x}/NC-900, and Fe_3O_{4-x}/NC-800. Note that the Fe_3O_{4-x}/NC-1000 sample was prepared with 200 cycles of PE-ALD deposition of Fe_3O_4, and the ORR performance in both 0.1 M KOH and 0.5 M H_2SO_4 was markedly better than those of the comparative samples that were prepared with less or more Fe_3O_4 deposition (Figure S18, Supporting Information). This suggests that 200 cycles of Fe_3O_4 deposition represented the optimal loading.

The fact that Fe_3O_{4-x}/NC-1000 exhibits the best electrocatalytic performance among the series can be ascribed to the highest concentration of oxygen vacancy, as attested in the above EPR measurements (Figure 3c). Oxygen vacancies have been known to increase the electron density and the formation of electron holes around the transitional metal centers, which can impact the electrical conductivity in the bulk and molecular adsorption on the surface.[23c,31] Mechanistically, the delocalized electrons can be readily excited to the conduction band, which effectively diminishes the band gap and enhance the electrical conductivity.[31a,d,e] The enhanced electron density can also facilitate the adsorption of oxygen intermediates onto the catalyst surface and hence the OER/ORR electrolysis,[23c,31e] as oxygen vacancies can promote electron transfer between the adsorbates and surface active sites, an important step for ORR/OER.[31d]

Remarkably, Fe_3O_{4-x}/NC-1000 outperformed relevant catalysts toward alkaline ORR reported recently in the literature (Table S3, Supporting Information),[24,32] and displayed its superiority even in the acidic media, which is rarely seen for iron oxide–carbon nanocomposites. Such an excellent ORR performance in both acidic and alkaline media may be accounted for by the combined contributions of the ready accessibility of the Fe_3O_{4-x} catalytic active sites and the surface oxygen vacancies, with additional contributions from the N-doped graphitic carbon frameworks. First, the PE-ALD deposition of Fe_3O_4 onto the 2D planar surface of the leaf-shaped ZIF precursors allows surface-enrichment of defective Fe_3O_{4-x} on the carbon scaffold and hence ready accessibility of the electrocatalytic active centers in the final nanocomposites. Second, as mentioned above, the oxygen vacancies can enhance the electrical conductivity, oxygen adsorption and electron-transfer kinetics. Finally, the N-doped graphitic carbon framework with charge redistribution can provide a favorable transfer medium for the protons and electrons, and further be used as a matrix to anchor Fe_3O_{4-x} few-atom clusters with high electronegative N heteroatoms.

2.3. Zinc–Air Battery

With the outstanding ORR performance, Fe_3O_{4-x}/NC-1000 was tested as the oxygen catalyst for ZAB. **Figure 5**a shows the schematic diagram of a ZAB, which was assembled by using the Fe_3O_{4-x}/NC-1000 sample as the air cathode catalyst, a 6.0 M KOH and 0.2 M zinc acetate aqueous solution as the electrolyte, and a polished zinc foil as the anode. As shown in Figure S19, Supporting Information, the resulting Fe_3O_{4-x}/NC-1000 based ZAB displayed a stable open circuit voltage of 1.430 V, somewhat higher than that based on a commercial Pt/C electrode (1.400 V), and it remained stable for 20 h. A typical discharge test displayed a maximum power density of 158 mW cm^{-2} with the former, better than that with the latter (145 mW cm^{-2}) (Figure 5b). As shown in Figure 5c, when the discharge was carried out at a constant current density of 10 mA cm^{-2}, the Fe_3O_{4-x}/NC-1000-based ZAB showed a specific capacity of 691 mA h g^{-1}, comparable to that with commercial Pt/C (682 mA h g^{-1}). The discharge curves under a larger current density of 50 and 100 mA cm^{-2} were acquired and are shown in Figure S20, Supporting Information. The rate performance was evaluated at the current densities of 1, 2, 5, 10, 20, 30, 50, and 100 mA cm^{-2}, and the Fe_3O_{4-x}/NC-1000 based ZAB again showed a clearly higher and more stable voltage than that with commercial Pt/C (Figure 5d). The cycling durability was then tested at the constant current density of 5 mA cm^{-2} for 2000 charge and discharge cycles over 600 h, and the former was much more stable than the latter (Figure 5e). Remarkably, the former ZAB also showed no obvious potential attenuation even at the high current density of 10 mA cm^{-2} during charge and discharge cycles for 750 h, as compared to the latter (Figure S21, Supporting Information). In fact, the Fe_3O_{4-x}/NC-1000 based ZAB clearly outperformed a number of relevant catalysts reported recently in the literature (Table S4, Supporting Information). Notably, two Fe_3O_{4-x}/NC-1000 based ZABs connected in series can light up a group of LED lights (Figure S22, Supporting Information). Taken together, these results suggest that Fe_3O_{4-x}/NC-1000 can be used as a high-performance air cathode catalyst for ZAB.

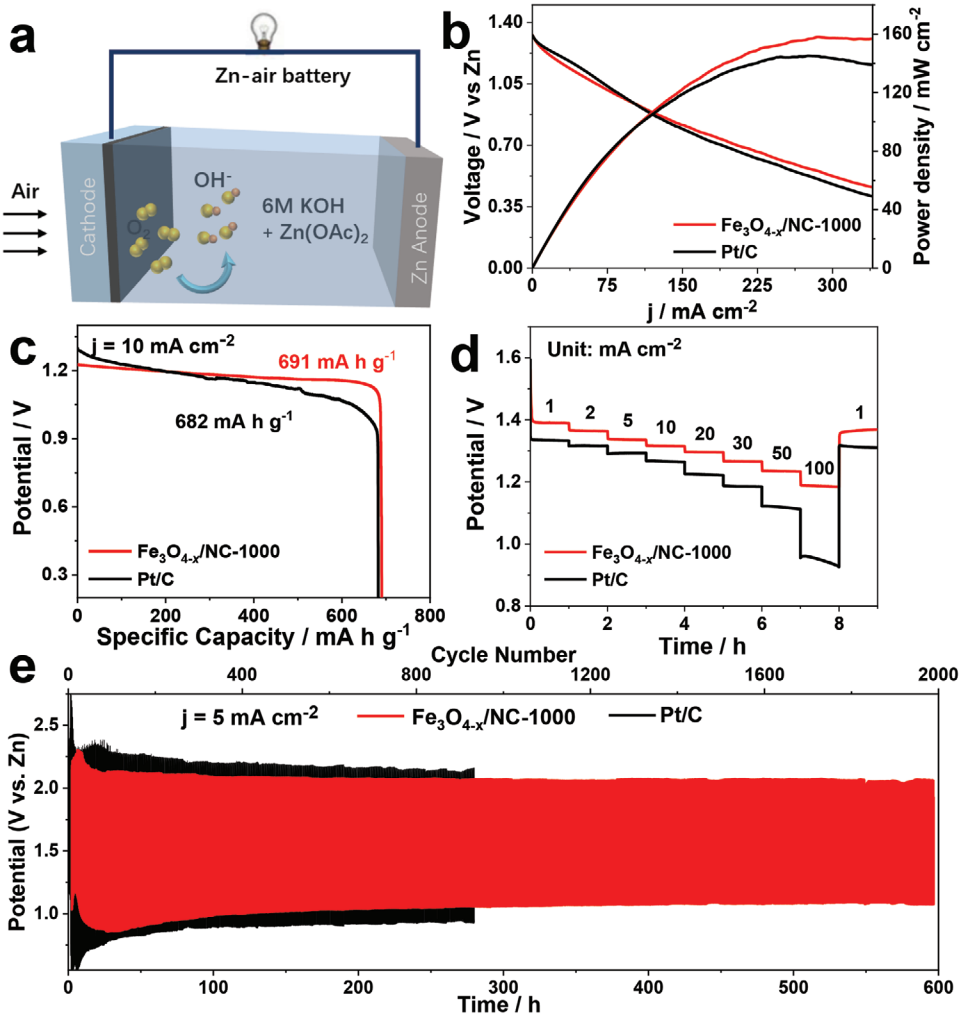

Figure 5. a) Schematic illustration of a Zn–air battery. Electrochemical performances of ZABs with Fe_3O_{4-x}/NC-1000 and commercial Pt/C as the air cathode catalysts: b) Polarization curves and corresponding power density plots (scan rate, 10 mV s^{-1}), c) discharge curves at 10 mA cm^{-2}, d) rate performance, and e) cycle stability at 5 mA cm^{-2}.

3. Conclusion

In summary, atomic layer deposition was employed to deposit a layer of Fe_3O_4 onto the surface of a ZIF precursor, and controlled pyrolysis at elevated temperatures led to the successful formation of carbon nanocomposites decorated with defective few-atom Fe_3O_{4-x} clusters. Electrochemical studies showed that the samples exhibited apparent electrocatalytic activity toward ORR in both acidic and alkaline media, and the one prepared at 1000 °C (Fe_3O_{4-x}/NC-1000) represented the optimal catalyst, with a performance comparable or even superior to that of commercial Pt/C, due to the high density of Fe_3O_{4-x} active sites and defect structures generated by abundant oxygen vacancies. When Fe_3O_{4-x}/NC-1000 was used as the cathode catalysts of a zinc–air battery, the device displayed a high open circuit voltage of 1.43 V, a high specific capacity of 691 mA h g^{-1}, a power density of 158 mW cm^{-2}, and stable cycle performance (600 h for 2000 cycles at 5 mA cm^{-2}). Results from this work highlight the unique advantages of atomic layer deposition in the preparation of high-performance catalysts for zinc–air battery.

Supporting Information

Supporting Information is available from the Wiley Online Library or from the author.

Acknowledgements

P.C. and Y.Z. contributed equally to this work. This work was financially supported by the National Natural Science Foundation of China (21471100, 22005199), the Shenzhen Natural Science Fund (the Stable Support Plan Program 20200813081943001), and the Guangdong Basic and Applied Basic Research Foundation (2021A1515010241, 2021A1515010142). The authors also acknowledge the technical assistance in STEM measurements from the Electron Microscopy Center of the Shenzhen University. S.C. acknowledges partial support from the US National Science Foundation (CHE-1900235 and CHE-2003685).

Conflict of Interest

The authors declare no conflict of interest.

Data Availability Statement

The data that support the findings of this study are available from the corresponding author upon reasonable request.

Keywords

Fe_3O_{4-x} clusters, oxygen reduction reaction, oxygen vacancies, plasma-enhanced atomic layer deposition, zinc–air batteries

Received: February 18, 2022
Revised: May 1, 2022
Published online:

[1] a) Z. Zhu, H. Yin, Y. Wang, C. H. Chuang, L. Xing, M. Dong, Y. R. Lu, G. Casillas-Garcia, Y. Zheng, S. Chen, Y. Dou, P. Liu, Q. Cheng, H. Zhao, *Adv. Mater.* **2020**, *32*, 2004670; b) N. Xu, J. A. Wilson, Y.-D. Wang, T. Su, Y. Wei, J. Qiao, X.-D. Zhou, Y. Zhang, S. Sun, *Appl. Catal. B: Environ.* **2020**, *272*, 118953; c) Y. M. Zhang, S. J. Li, L. L. Cheng, Y. L. Li, X. Z. Ren, P. X. Zhang, L. N. Sun, H. Y. Yang, *J. Mater. Chem. A* **2021**, *9*, 3388.

[2] a) D. C. Nguyen, D. T. Tran, T. L. L. Doan, D. H. Kim, N. H. Kim, J. H. Lee, *Adv. Energy Mater.* **2020**, *10*, 1903289; b) Y. M. Zhang, H. N. Li, S. Z. Huang, S. Fan, L. N. Sun, B. B. Tian, F. M. Chen, Y. Wang, Y. M. Shi, H. Y. Yang, *Nano-Micro Lett.* **2020**, *12*, 60; c) T. T. Wang, Z. K. Kou, S. C. Mu, J. P. Liu, D. P. He, I. S. Amiinu, W. Meng, K. Zhou, Z. X. Luo, S. Chaemchuen, F. Verpoort, *Adv. Funct. Mater.* **2018**, *28*, 1705048.

[3] a) J. Zhu, M. Xiao, G. Li, S. Li, J. Zhang, G. Liu, L. Ma, T. Wu, J. Lu, A. Yu, D. Su, H. Jin, S. Wang, Z. Chen, *Adv. Energy Mater.* **2019**, *10*, 1903003; b) L. Ye, M. Liao, H. Sun, Y. F. Yang, C. Q. Tang, Y. Zhao, L. Wang, Y. F. Xu, L. J. Zhang, B. J. Wang, F. Xu, X. M. Sun, Y. Zhang, H. J. Dai, P. G. Bruce, H. S. Peng, *Angew. Chem., Int. Ed.* **2019**, *58*, 2437.

[4] a) S. J. Guo, S. Zhang, S. H. Sun, *Angew. Chem., Int. Ed.* **2013**, *52*, 8526; b) V. Petrykin, K. Macounova, O. A. Shlyakhtin, P. Krtil, *Angew. Chem., Int. Ed.* **2010**, *49*, 4813; c) L. Zu, X. Qian, S. Zhao, Q. Liang, Y. E. Chen, M. Liu, B. J. Su, K. H. Wu, L. Qu, L. Duan, H. Zhan, J. Y. Zhang, C. Li, W. Li, J. Y. Juang, J. Zhu, D. Li, A. Yu, D. Zhao, *J. Am. Chem. Soc.* **2022**, *144*, 2208.

[5] a) Y. Wang, Q. Cao, C. Guan, C. Cheng, *Small* **2020**, *16*, 2002902; b) Y. Lei, F. Yang, H. Xie, Y. Lei, X. Liu, Y. Si, H. Wang, *J. Mater. Chem. A* **2020**, *8*, 20629; c) K. Zeng, X. Zheng, C. Li, J. Yan, J.-H. Tian, C. Jin, P. Strasser, R. Yang, *Adv. Funct. Mater.* **2020**, *30*, 2000503.

[6] L. Huo, B. Liu, G. Zhang, R. Si, J. Liu, J. Zhang, *J. Mater. Chem. A* **2017**, *5*, 4868.

[7] R. Hao, J.-T. Ren, X.-W. Lv, W. Li, Y.-P. Liu, Z.-Y. Yuan, *J. Energ. Chem.* **2020**, *49*, 14.

[8] H.-x. Zhong, J. Wang, Y.-w. Zhang, W.-l. Xu, W. Xing, D. Xu, Y.-f. Zhang, X.-b. Zhang, *Angew. Chem., Int. Ed.* **2014**, *53*, 14235.

[9] a) S. Yuan, J. Peng, B. Cai, Z. Huang, A. T. Garcia-Esparza, D. Sokaras, Y. Zhang, L. Giordano, K. Akkiraju, Y. G. Zhu, R. Hubner, X. Zou, Y. Roman-Leshkov, Y. Shao-Horn, *Nat. Mater.* **2022**, https://doi.org/10.1038/s41563-022-01199-0; b) L. Jiao, J. Zhu, Y. Zhang, W. Yang, S. Zhou, A. Li, C. Xie, X. Zheng, W. Zhou, S. H. Yu, H. L. Jiang, *J. Am. Chem. Soc.* **2021**, *143*, 19417.

[10] a) Y. Jiang, Y. P. Deng, R. L. Liang, N. Chen, G. King, A. P. Yu, Z. W. Chen, *J. Am. Chem. Soc.* **2022**, *144*, 4783; b) H. Park, S. Oh, S. Lee, S. Choi, M. Oh, *Appl. Catal. B: Environ.* **2019**, *246*, 322.

[11] J. Wang, G. Han, L. Wang, L. Du, G. Chen, Y. Gao, Y. Ma, C. Du, X. Cheng, P. Zuo, G. Yin, *Small* **2018**, *14*, 1704282.

[12] G. Li, J. Zhang, W. Li, K. Fan, C. Xu, *Nanoscale* **2018**, *10*, 9252.

[13] M. H. Zhang, E. H. Zhang, C. Y. Hu, Y. Zhao, H. M. Zhang, Y. J. Zhang, M. W. Ji, J. L. Yu, G. T. Cong, H. C. Liu, J. T. Zhang, C. Z. Zhu, J. Xu, *ACS Appl. Mater. Interfaces* **2020**, *12*, 11693.

[14] Y. Zhao, L. Zhang, J. Liu, K. Adair, F. P. Zhao, Y. P. Sun, T. P. Wu, X. X. Bi, K. Amine, J. Lu, X. L. Sun, *Chem. Soc. Rev.* **2021**, *50*, 3889.

[15] Q. M. Liu, Y. Peng, Q. X. Li, T. He, D. Morris, F. Nichols, R. Mercado, P. Zhang, S. W. Chen, *ACS Appl. Mater. Interfaces* **2020**, *12*, 17641.

[16] a) H. Li, Z. Guo, X. Wang, *J. Mater. Chem. A* **2017**, *5*, 21353; b) K. L. Pickrahn, S. W. Park, Y. Gorlin, H.-B.-R. Lee, T. F. Jaramillo, S. F. Bent, *Adv. Energy Mater.* **2012**, *2*, 1269.

[17] a) B. T. Qiao, A. Q. Wang, X. F. Yang, L. F. Allard, Z. Jiang, Y. T. Cui, J. Y. Liu, J. Li, T. Zhang, *Nat. Chem.* **2011**, *3*, 634; b) K. L. Nardi, N. Yang, C. F. Dickens, A. L. Strickler, S. F. Bent, *Adv. Energy Mater.* **2015**, *5*, 1500412; c) X. Zhou, R. Liu, K. Sun, K. M. Papadantonakis, B. S. Brunschwigad, N. S. Lewis, *Energy Environ. Sci.* **2015**, *9*, 892.

[18] X. Yang, X. Sun, L.-Y. Gan, L. Sun, H. Mi, P. Zhang, X. Ren, Y. Li, *J. Mater. Chem. A* **2020**, *8*, 15140.

[19] Y. M. Zhang, Y. V. Lim, S. Z. Huang, M. E. Pam, Y. Wang, L. K. Ang, Y. M. Shi, H. Y. Yang, *Small* **2018**, *14*, 1800898.

[20] a) J. Han, X. Meng, L. Lu, J. Bian, Z. Li, C. Sun, *Adv. Funct. Mater.* **2019**, *29*, 1808872; b) Q. Hu, Z. Han, X. D. Wang, G. M. Li, Z. Y. Wang, X. W. Huang, H. P. Yang, X. Z. Ren, Q. L. Zhang, J. H. Liu, C. X. He, *Angew. Chem., Int. Ed.* **2020**, *59*, 19054.

[21] Z. Wang, J. Ang, B. Zhang, Y. Zhang, X. Y. D. Ma, J. L. Tao Yanb, B. Che, Y. Huang, X. Lua, *Appl. Catal.,B.* **2019**, *254*, 26.

[22] B. Z. Lu, Q. M. Liu, F. Nichols, R. Mercado, D. Morris, N. Li, P. Zhang, P. Gao, Y. Ping, S. W. Chen, *Research* **2020**, *2020*, 9167829.

[23] a) P. Krishnan, M. Liu, P. A. Itty, Z. Liu, V. Rheinheimer, M.-H. Zhang, P. J. M. Monteiro, L. E. Yu, *Sci. Rep.* **2017**, *7*, 43298; b) H. Idriss, *Surf. Sci.* **2021**, *712*, 121894; b) L. Gao, C. Tang, J. Liu, L. He, H. Wang, Z. Ke, W. Li, C. Jiang, D. He, L. Cheng, X. Xiao, *Energy Environ. Mater.* **2021**, *4*, 392.

[24] a) Y. J. Deng, X. L. Tian, G. H. Shen, Y. Gao, C. X. Lin, L. M. Ling, F. L. Cheng, S. J. Liao, S. G. Zhang, *J. Colloid Interface Sci.* **2020**, *567*, 410; b) Y. P. Liu, B. Qiao, N. Jia, S. F. Shi, X. B. Chen, Z. W. An, P. Chen, *ChemCatChem* **2022**, *14*, e202101523.

[25] Y. Chen, Z. Li, Y. Zhu, D. Sun, X. Liu, L. Xu, Y. Tang, *Adv. Mater.* **2019**, *31*, 1806312.

[26] S. Zeng, F. Lyu, H. Nie, Y. Zhan, H. Bian, Y. Tian, Z. Li, A. Wang, J. Lu, Y. Y. Li, *J. Mater. Chem. A* **2017**, *5*, 13189.

[27] B. Lei, D. D. Xu, B. Wei, T. F. Xie, C. Y. Xiao, W. L. Jin, L. L. Xu, *ACS Appl. Mater. Interfaces* **2021**, *13*, 4785.

[28] F. Xiao, G.-L. Xu, C.-J. Sun, M. Xu, W. Wen, Q. Wang, M. Gu, S. Zhu, Y. Li, Z. Wei, X. Pan, J. Wang, K. Amine, M. Shao, *Nano Energy* **2019**, *61*, 60.

[29] Y. Li, J. W. Li, J. H. Huang, J. X. Chen, Y. Kong, B. Yang, Z. J. Li, L. C. Lei, G. L. Chai, Z. H. Wen, L. M. Dai, Y. Hou, *Angew. Chem., Int. Ed.* **2021**, *60*, 9078.

[30] J. Han, H. Bao, J.-Q. Wang, L. Zheng, S. Sun, Z. L. Wang, C. Sun, *Appl. Catal.,B.* **2021**, *280*, 119411.

[31] a) Y. M. Zhang, L. X. Feng, W. T. Zhan, S. J. Li, Y. L. Li, X. Z. Ren, P. X. Zhang, L. N. Sun, *ACS Appl. Energy Mater.* **2020**, *3*, 4014; b) W. Jian, S.-P. Wang, H.-X. Zhang, F.-Q. Bai, *Inorg. Chem. Front.* **2019**, *6*, 2660; c) H. Jin, X. Tian, Y. Nie, Z. Zhou, C. Yang, Y. Li, L. Lu, *Environ. Sci. Technol.* **2017**, *51*, 12699; d) Q. Ji, L. Bi, J. Zhang, H. Cao, X. S. Zhao, *Energy Environ. Sci.* **2020**, *13*, 1408; e) K. Y. Zhu, F. Shi, X. F. Zhu, W. S. Yang, *Nano Energy* **2020**, *73*, 1408.

[32] a) Z. H. Yao, Y. T. Li, D. S. Chen, Y. W. Zhang, X. H. Bao, J. Wang, Q. Zhong, *Chem. Eng. J.* **2021**, *415*, 129033; b) R. H. Gan, Y. L. Wang, W. J. Ma, M. Dirican, S. Zhao, Y. Song, X. W. Zhang, C. Ma, J. L. Shi, *Int. J. Hydrogen Energy* **2022**, *47*, 2103.